



GLOBAL JOURNAL OF RESEARCHES IN ENGINEERING: F  
ELECTRICAL AND ELECTRONICS ENGINEERING  
Volume 15 Issue 5 Version 1.0 Year 2015  
Type: Double Blind Peer Reviewed International Research Journal  
Publisher: Global Journals Inc. (USA)  
Online ISSN: 2249-4596 & Print ISSN: 0975-5861

# Multi-Body Dynamic Modeling and Simulation of Crawler-Formation Interactions in Surface Mining Operations - Crawler Kinematics

By Samuel Frimpong & Magesh Thiruvengadam

*Missouri University of Science and Technology, United States*

**Abstract-** Surface mining operations use large tracked shovels to achieve economic bulk production capacities. Shovel reliability, maintainability, availability and efficiency depend on the service life of the crawlers. In rugged and challenging terrains, the extent of crawler wear, tear, cracks and fatigue failure can be extensive resulting in prolonged downtimes with severe economic implications. In particular, crawler shoe wear, tear, cracks and fatigue failures can be expensive in terms of maintenance costs and production losses. This research study is a pioneering effort for understanding and providing long-term solutions to crawler-formation problems in surface mining applications. The external forces acting on the crawler shoes and oil sand are formulated to determine system kinematics. The dynamic model focuses on the external force from machine weight, the crawler contact forces, the contact friction forces and the inertia and gravity forces using multi-body dynamics theory. A virtual prototype simulator of the crawler dynamics is simulated within the MSC ADAMS environment.

**Keywords:** *surface mining, crawler-terrain interactions, multi-body dynamic theory, crawler dynamic modeling, virtual prototype simulation.*

**GJRE-F Classification :** FOR Code: 090699



*Strictly as per the compliance and regulations of :*



RESEARCH | DIVERSITY | ETHICS

© 2015. Samuel Frimpong & Magesh Thiruvengadam . This is a research/review paper, distributed under the terms of the Creative Commons Attribution-Noncommercial 3.0 Unported License (<http://creativecommons.org/licenses/by-nc/3.0/>), permitting all non commercial use, distribution, and reproduction in any medium, provided the original work is properly cited.

# Multi-Body Dynamic Modeling and Simulation of Crawler-Formation Interactions in Surface Mining Operations – Crawler Kinematics

Samuel Frimpong <sup>α</sup> & Magesh Thiruvengadam <sup>σ</sup>

**Abstract-** Surface mining operations use large tracked shovels to achieve economic bulk production capacities. Shovel reliability, maintainability, availability and efficiency depend on the service life of the crawlers. In rugged and challenging terrains, the extent of crawler wear, tear, cracks and fatigue failure can be extensive resulting in prolonged downtimes with severe economic implications. In particular, crawler shoe wear, tear, cracks and fatigue failures can be expensive in terms of maintenance costs and production losses. This research study is a pioneering effort for understanding and providing long-term solutions to crawler-formation problems in surface mining applications. The external forces acting on the crawler shoes and oil sand are formulated to determine system kinematics. The dynamic model focuses on the external force from machine weight, the crawler contact forces, the contact friction forces and the inertia and gravity forces using multi-body dynamics theory. A virtual prototype simulator of the crawler dynamics is simulated within the MSC ADAMS environment. The simulation results for kinematics (displacement, velocities and accelerations) of selected crawler track shoes are presented. The results show that during translation motion, the track's maximum lateral slide and vertical bounce from the equilibrium position are 1 cm and 3.5 cm respectively. The corresponding magnitudes of maximum lateral and bouncing velocities and accelerations are about 0.06 m/s and 0.45 m/s and 1.8 m/s<sup>2</sup> and 27.0 m/s<sup>2</sup> respectively. The crawler track also rotates while translating with angular velocities about x, y and z axes reaching maximum magnitudes of 12.5 deg/s, 73.0 deg/s and 1.6 deg/s. During the turning motion, the crawler track experiences varying bouncing and rolling motions causing its maximum lateral velocity to increase 5 times and vertical bouncing velocities to increase 9 times the maximum values encountered during translation. This study provides guidelines to simulate flexible crawler track-bench interactions in oil-sand mine for predicting and improving fatigue life during dynamic loading of the crawler shoes.

**Keywords:** surface mining, crawler-terrain interactions, multi-body dynamic theory, crawler dynamic modeling, virtual prototype simulation.

## I. INTRODUCTION

Cable shovels are widely used in surface mining operations. The lower works of this shovel comprise propel and crawler systems, which

The crawler tracks are made up of shoes that are connected together by link pins to form a continuous chain [2]. Multi-body dynamics study on crawler-terrain interactions is non-existent for large shovels in surface mining operations but it is required to provide knowledge of crawler performance and fatigue life. Fatigue life modeling and analysis are also required to develop preventive maintenance plans, component replacements and rebuilds to extend the life of the crawlers and reduce their maintenance costs. Nakanishi and Shabana (1994) used a 2-D hydraulic excavator model to study the multi-body dynamics of a tracked vehicle. The track interaction with sprockets, rollers and ground were modeled using the spring-damper force to calculate the track-terrain normal contact forces. The tangential force was modeled using a simple Coulomb friction model. Choi et al. (1998) and Lee et al. (1998) extended the 2-D study of Nakanishi and Shabana (1994) to a 3-D contact force models of a hydraulic excavator.

*Author α:* Professor and Robert Quenon Chair, Missouri University of Science and Technology, Rolla. e-mail: frimpong@mst.edu

*Author σ:* Research Assistant Professor, Missouri University of Science and Technology, Rolla.



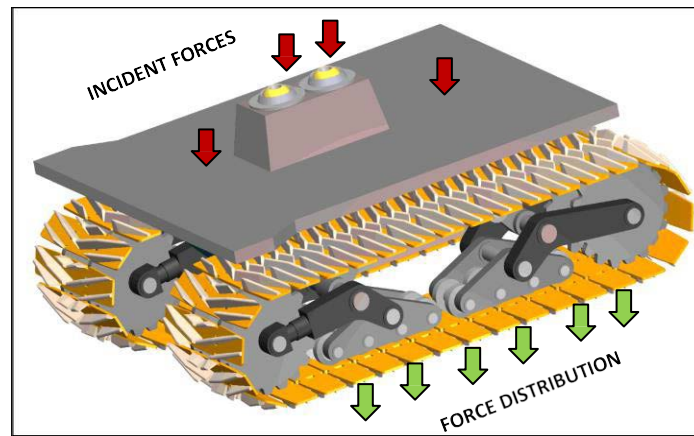


Figure 1: 4100C BOSS Electric Mining Shovel [1]

Rubinstein and Hitron (2004) used an LMS-DADS simulation to develop a multi-body dynamic M113 armored carrier tracked vehicle simulator. Hertz theory was used to model the track- terrain contact force, and user-defined force elements to calculate normal and tangential forces between the track and the terrain. Rubinstein and Coppock (2007) extended this model by including grousers in the track-terrain model. Ferretti and Girelli (1999) developed a 3-D dynamic model of an agricultural tracked vehicle using Newton-Euler rigid-body theory. They introduced a track-terrain model using soil mechanics theory to generate the dynamics of the system. They used these parameters as input in the dynamic model to calculate sinkage and shear displacement of the track.

Ryu et al. (2000) developed a computational method for a non-linear dynamic model of military tracked vehicle. They used compliant force elements between the pins and track links to increase the degrees of freedom (DOF) based on the track-terrain contact force model by Choi et al. (1998). Madsen (2007) used MSC ADAMS to simulate a complex tracked hydraulic excavator. The model used the contact force model in ADAMS to define the crawler-terrain interactions. Ma and Perkins (1999) developed a hybrid track model for a large mining shovel crawler using continuous and multi-body track model. A commercial multi-body dynamics code, DADS, was used to assemble the continuous and multi-body track vehicle model. Their study was limited to studying a 2-D dynamic contact between track and sprocket during the propel motion.

Previous research on multi-body dynamic models has also focused on shovel dipper-bank interactions. Frimpong et al. (2005) used an iterative Newton-Euler method to develop a dynamic model of

boom, dipper handle and dipper assembly. Their dynamic model identified the important factors that determine the performance of the shovel during its digging phase. Frimpong and Li (2007) also modeled the interaction between the dipper of a cable shovel and oil sands formation using multi-body dynamics theory. In addition, the shovel boom was made flexible to determine its deformation and stress distribution during shovel operations.

Frimpong and Thiruvengadam (2015) have formulated the kinematics of the crawler-flexible terrain interactions of a large mining shovel in surface mining operations (P&H 4100C BOSS Electric Shovel in Figure 1). They showed that 132 DOFs in the crawler-terrain system are driven by external forces and dynamic analysis is required to generate the remaining DOFs. This paper advances the kinematic models to formulate the dynamic models for the crawler-terrain interactions based on the rigid multi-body dynamics theory [14, 15, 16 and 17].

## II. RIGID MULTI-BODY DYNAMICS OF CRAWLER-TERRAIN INTERACTIONS

Figure 2 illustrates the geometry of the crawler track assemblies for the P&H 4100C Boss shovel. The track is modeled using the crawler track dimensions given in Table 1. Only the open track chain of the crawler assembly, in contact with the ground (Figure 1), is used for this study. Since the crawler track is made up of crawler shoes, a simplified crawler shoe model is developed first and then connected together to form the multi-body model of track assembly. This simplified model is generated in Solidworks based on the actual crawler shoe model for P&H 4100C Boss shovel [18].

Table 1: Mass properties of system [13, 18]

Body	Density (kg/m <sup>3</sup> )	Volume (m <sup>3</sup> )	Mass (kg)
Crawler Shoe	7847.25	0.5966	4681.67
Oil-sand unit	1600.0	98.0	1.568 x 10 <sup>5</sup>

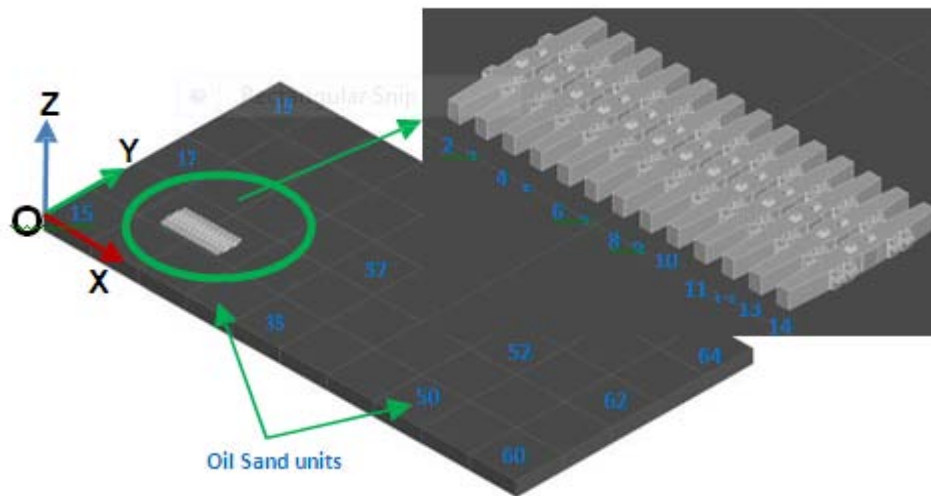


Figure 2 : Crawler track assembly interacting with the ground

The mass moment of inertia of each body in the system used for the dynamic analysis [19, 20 and 21] is obtained directly from MSC ADAMS. The crawler shoes 2-14 are identical and all of them have the same mass moment of inertia about their centers of mass.

### III. DYNAMIC EQUATIONS OF MOTION

The shovel weight ( $W$ ), supported by two crawlers, is uniformly distributed on the crawler shoes that are in contact with the ground [2]. This study

focuses only on the crawler shoes in contact with the ground for one crawler track. This crawler track segment along with one half of the vehicle load ( $W/2$ ) acting on it is shown in Figure 3. From Wong (2001), when the vehicle sinks vertically to the ground the ground exerts normal force ( $F_N$ ), and tangential force ( $F_T$ ) (longitudinal and lateral) on the crawler track segment as shown in Figure 3. These normal and tangential forces are modeled using inbuilt contact force mechanism in MSC ADAMS.

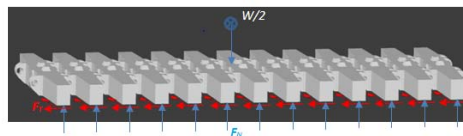


Figure 3 : Ground Forces acting on the shovel crawler track

*Crawler shoes dynamic equilibrium for link  $i$ :* In the multi-body model shown in Figure 2, the weight ( $W/2$ ) is assumed to be equally shared by thirteen crawler shoes. The uniformly distributed load ( $w$ ) applied on each shoe is in addition to its self-weight. The mass of the crawler shoe is assumed as  $m_i$ . The free body diagram of a crawler shoe  $i$  with inertia forces in dynamic equilibrium with external and joint constraint forces is shown in Figure 4 [14, 22 and 23]. The external forces acting on the crawler shoe #  $i$  are the gravity force ( $m_i g$ ) due to selfweight of the shoe, uniformly distributed load ( $w$ ) due to machine weight and contact forces ( $F_C^i, M_C^i$ ) due to the interaction between crawler shoe and ground as shown in Figure 3. The joint forces are due to reactive forces at the spherical joints ( $F_S^{i-1,i}, M_S^{i-1,i}$  and  $F_S^{i,i+1}, M_S^{i,i+1}$ ) and parallel primitive joints ( $F_P^{i-1,i}, M_P^{i-1,i}$  and  $F_P^{i,i+1}, M_P^{i,i+1}$ ) as shown in Figure 4.

The following dynamic equation of motion uses the notations and formulation described in Shabana [14, 15]. The dynamic equations of motion for the constrained rigid body  $i$  using centroidal body coordinate system from Shabana [14, 15] is given by equation (1).

$$\mathbf{M}^i \ddot{\mathbf{q}}^i - \mathbf{Q}_v^i = \mathbf{Q}_e^i + \mathbf{Q}_c^i \quad (1)$$

$i = 2, 3, \dots, 14$  for crawler shoes and  $i = 15, 16, \dots, 64$  for oil sand units.

*Generalized Inertia Forces of Crawler shoe  $i = 2, 3, \dots, 14$ :* The generalized inertia force is given by the left hand side of the equation 1. From Shabana [14, 15]

$$\mathbf{M}^i = \begin{bmatrix} \mathbf{m}_{RR}^i & \mathbf{0} \\ \mathbf{0} & \mathbf{m}_{\theta\theta}^i \end{bmatrix} = \text{Mass matrix of the crawler shoe } i \quad (2)$$

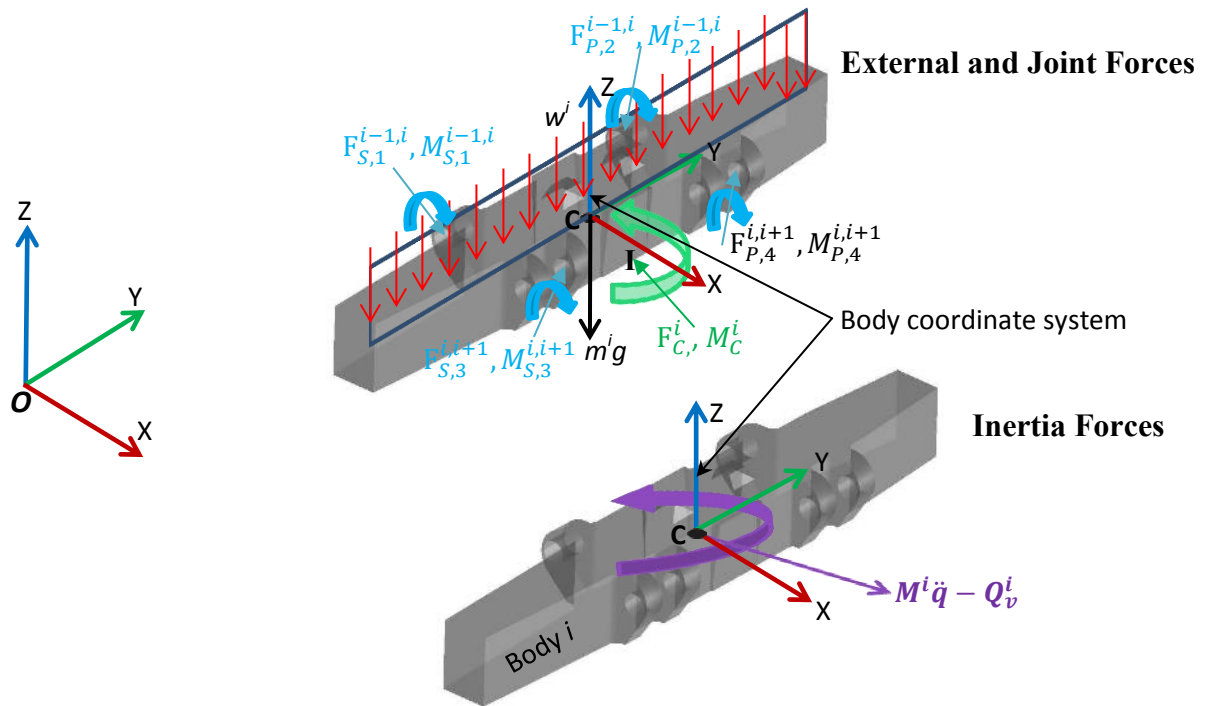


Figure 4 : Dynamic equilibrium of the rigid crawler shoe

$$\mathbf{Q}_v^i = \begin{bmatrix} 0 \\ (\mathbf{Q}_v^i)_\theta \end{bmatrix} = \text{Vector of generalized quadratic velocity vector} \quad (3)$$

$$\ddot{\mathbf{q}}^i = [\ddot{R}_x^i \quad \ddot{R}_y^i \quad \ddot{R}_z^i \quad \ddot{\phi}^i \quad \ddot{\theta}^i \quad \ddot{\psi}^i]^T = \text{of generalized acceleration of body} \quad (4)$$

$$\mathbf{m}_{RR}^i = \begin{bmatrix} m^i & \mathbf{0} & \mathbf{0} \\ \mathbf{0} & m^i & \mathbf{0} \\ \mathbf{0} & \mathbf{0} & m^i \end{bmatrix} \quad (5)$$

$$\mathbf{m}_{\theta\theta}^i = \bar{\mathbf{G}}^{iT} \bar{\mathbf{I}}_{\theta\theta}^i \bar{\mathbf{G}}^i \quad (6)$$

$$(\mathbf{Q}_v^i)_\theta = -\bar{\mathbf{G}}^{iT} [\bar{\boldsymbol{\omega}}^i \times (\bar{\mathbf{I}}_{\theta\theta}^i \bar{\boldsymbol{\omega}}^i) + \bar{\mathbf{I}}_{\theta\theta}^i \dot{\bar{\boldsymbol{\theta}}}^i] \quad (7)$$

Equation (7) is the generalized quadratic velocity vector associated with the orientation coordinates  $(\boldsymbol{\theta})$ . In equation (7),

$$\bar{\mathbf{G}}^i = \begin{bmatrix} \sin \theta^i \sin \psi^i & \cos \psi^i & 0 \\ \sin \theta^i \cos \psi^i & \sin \psi^i & 0 \\ \cos \theta^i & 0 & 1 \end{bmatrix} \quad (8)$$

$$\bar{\boldsymbol{\omega}}^i = \bar{\mathbf{G}}^i \dot{\boldsymbol{\theta}}^i \quad (9)$$

$$\bar{\mathbf{I}}_{\theta\theta}^i = \begin{bmatrix} I_{XX} & I_{XY} & I_{XZ} \\ I_{YX} & I_{YY} & I_{YZ} \\ I_{ZX} & I_{ZY} & I_{ZZ} \end{bmatrix} \quad (10)$$

Equation (8) is the unit vectors along the x, y, z axis of the centroidal coordinate system of body  $i$ ; and  $\bar{\mathbf{I}}_{\theta\theta}^i =$  inertia tensor [14, 22 and 23] of shoe  $i$  in its centroidal coordinate system aligned with global coordinate system shown in Figure 2. Equation (9) is the angular velocity vector in the body coordinate system.

Generalized External Forces acting on crawler shoe  $i = 2, 3, \dots, 14$ : The first term on the RHS of equation (1) gives the generalized external forces in the crawler track multi-body system [14].

$$\mathbf{Q}_e^i = \begin{bmatrix} (\mathbf{Q}_e^i)_R \\ (\mathbf{Q}_e^i)_\theta \end{bmatrix} \quad (11)$$

$(\mathbf{Q}_e^i)_R$  is the vector of generalized applied forces associated with the translation coordinates  $\mathbf{R}$ ;

$(\mathbf{Q}_e^i)_\theta$  is the vector of generalized applied forces associated with the orientation coordinates  $\theta$ .

The gravity force, distributed machine load, and contact forces are the external forces acting on the crawler system. The generalized external forces are obtained from Shabana [14, 15].

The self-weight of the crawler shoe due to its mass ( $m^i$ ) acting at its centroid C is shown in Figure 4. The mass of the crawler shoe from Table 1 =  $m^i = 4681.67$  kg and the gravity force acting at the center of mass of each crawler shoe =  $m^i g = 432.3$  kN. The gravity force vector ( $\mathbf{F}_g^i$ ) acting on each crawler shoe i in the global coordinate system =  $[0 \ 0 \ -m^i g]^T$ . The generalized forces, associated with the gravity force, are given as equations (12) and (13).

$$\mathbf{Q}_R^i = \begin{bmatrix} Q_x^i \\ Q_y^i \\ Q_z^i \end{bmatrix} = \mathbf{F}_g^i = \begin{bmatrix} 0 \\ 0 \\ -m^i g \end{bmatrix} \quad (12)$$

$$\mathbf{Q}_\theta^i = -(\mathbf{A}^i \tilde{\mathbf{u}}_C^i \mathbf{G}^i)^T \mathbf{F}_g^i \quad (13)$$

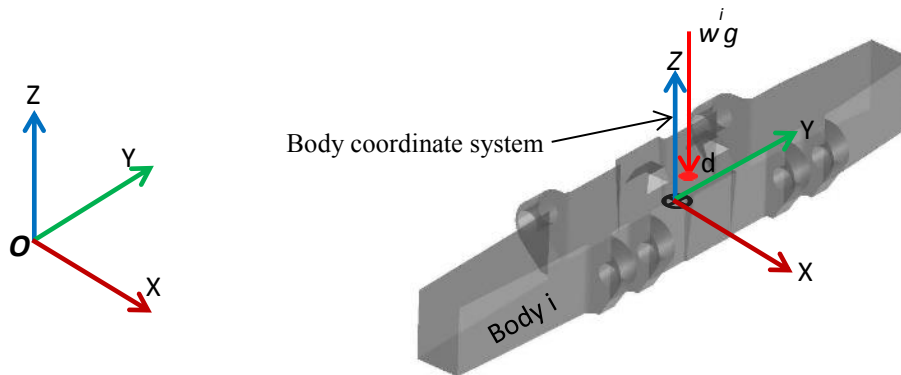


Figure 5: Equivalent distributed load on the crawler shoe

This distributed load can be represented by a single equivalent force ( $w^i g = 386.4$  kN) and is assumed to pass through the centroid (d) of the top surface of each crawler shoe i as shown in Figure 5. The distributed force vector ( $\mathbf{F}_d^i$ ) acting on each crawler shoe i in the global coordinate system =  $[0 \ 0 \ -w^i g]^T$ . The generalized forces associated with the

$$\tilde{\mathbf{u}}_C^i = \begin{bmatrix} 0 & -\bar{z}_c^i & \bar{y}_c^i \\ \bar{z}_c^i & 0 & -\bar{x}_c^i \\ -\bar{y}_c^i & \bar{x}_c^i & 0 \end{bmatrix} \quad (14)$$

$\mathbf{A}^i$  is a transformation matrix given in Frimpong and Thiruvengadam (2015); equation (14) is a skew symmetric matrix associated with the vector  $\bar{\mathbf{u}}_C^i$ ; and  $\bar{\mathbf{u}}_C^i = [\bar{x}_c^i \ \bar{y}_c^i \ \bar{z}_c^i]^T$  is the position vector of center of mass of body i with respect to the origin of the body coordinate system. Since the origin of the reference point of body i coincide with the center of the mass of body i, the vector  $\bar{\mathbf{u}}_C^i = \mathbf{0}$ . Therefore,  $\mathbf{Q}_\theta^i = \mathbf{0}$ . These generalized forces are added to the generalized external force vector  $\mathbf{Q}_e^i$  in equation (1).

The distributed load on each crawler shoe is due to the weight of the machine. The total machine load, excluding the weight of the crawler shoes in contact with the ground, is assumed to be distributed uniformly on each crawler shoe as shown in Figure 4. For example, the total machine weight [1] is 1,410,184 kg. Half of this weight is 705,092 kg. The total number of crawler shoes in contact with the ground (for the P&H 4100C BOSS) is 16, and thus, the total weight of 16 crawler shoe is 74,907 kg. Therefore the distributed weight ( $w^i$ ) on each crawler shoe in contact with the ground is equal to 39,387 kg. This research focuses on the total force and moment exerted by the distributed load.

distributed force from Shabana (2010) are given by equations (15) and (16).

$$\mathbf{Q}_R^i = \begin{bmatrix} Q_x^i \\ Q_y^i \\ Q_z^i \end{bmatrix} = \mathbf{F}_d^i = \begin{bmatrix} 0 \\ 0 \\ -w^i g \end{bmatrix} \quad (15)$$

$$\mathbf{Q}_\theta^i = -(\mathbf{A}^i \tilde{\mathbf{u}}_d^i \overline{\mathbf{G}}^i)^T \mathbf{F}_d^i \quad (16)$$

$\tilde{\mathbf{u}}_d^i = [\tilde{x}_d^i \ \tilde{y}_d^i \ \tilde{z}_d^i]^T$  is the position vector of point of application of equivalent force  $\mathbf{F}_d^i$  with respect to the origin of the body coordinate system. These generalized forces are added to the generalized external force vector  $\mathbf{Q}_e^i$  in equation (1).

Contact force between crawler shoe and ground: Figure 4 also shows the 3-D contact forces (normal and tangential) and the torque between track shoe i and ground [21, 24 and 25]. These forces will act on the crawler shoe bottom surface at a point I [28] as shown in Figure 4. The normal force ( $\mathbf{F}_N$ ) shown in Figure 6 is calculated using the impact function model in MSC ADAMS. In this model, when two solid bodies come in contact with each other a nonlinear spring damper system is introduced to determine the normal force [26, 27, 28 and 29].

$$\mathbf{F}_N^i = \begin{cases} kx^e - c_{\max} \dot{x} * \text{Step}(x, 0, 0, d, 1) & \text{if } x > 0 \\ 0 & \text{if } x \leq 0 \end{cases} \quad (17)$$

Table 2 : Friction Parameters used in the study [28, 29]

Static Friction Coefficient ( $\mu_s$ )	Dynamic Friction Coefficient ( $\mu_d$ )	Static Transition velocity ( $V_{st}$ , m)	Dynamic Transition velocity ( $V_d$ , m)
0.4	0.3	0.01	0.1

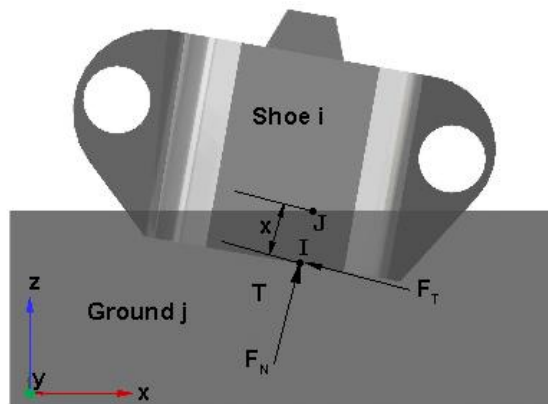


Figure 6 : Normal and Tangential Force and Torque calculations

The tangential force vector at contact point I is given by  $\mathbf{F}_T^i = [F_{T,x} \ F_{T,y} \ F_{T,z}]$ . The components of the tangential forces  $F_{T,x}$ ,  $F_{T,y}$  and  $F_{T,z}$  are calculated by substituting  $\mu$  obtained from friction coefficient-slip velocity relationship into equation 18 [28, 29]. The friction torque  $\mathbf{T}^i$  about the contact normal axis shown in Figure 6 impedes any relative rotation of shoe i with respect to the ground [29]. This torque is proportional to the friction force  $\mathbf{F}_T^i$  [29].

$k$  – stiffness of the spring =  $1 \times 10^8 \text{ N}$ ;  $m$   $x$  – penetration depth = distance variable used in the impact function model; and  $e$  – force exponent = 2.0.  $c_{\max}$  – maximum damping coefficient =  $1 \times 10^4 \text{ N-s/m}$  and  $d$  – penetration depth at which maximum damping is applied = 0.0001 m. The normal force vector acting at point I for the crawler shoe i is

$\mathbf{F}_N^i = [F_{N,x} \ F_{N,y} \ F_{N,z}]^T$ . The coulomb friction model in Adams is used for calculating tangential frictional force ( $\mathbf{F}_T$ ) shown in Figure 6. Based on this model, the frictional force acting at point I is calculated based on equation (18) [21, 25, 28 and 29].

$$\mathbf{F}_T^i = \mu(\mathbf{V}_s) \mathbf{F}_N^i \quad (18)$$

$\mu(\mathbf{V}_s)$  = friction coefficient defined as a function of slip velocity vector  $\mathbf{V}_s = [V_{s,x} \ V_{s,y} \ V_{s,z}]$  at contact point I [28, 29]. The friction parameters listed in Table 2 are used in the study for calculating tangential forces.

$$\mathbf{T}^i = \frac{2}{3} R \mathbf{F}_T^i \quad (19)$$

$R$  = radius of the contact area [29]. The generalized forces associated with contact force vector at point I ( $\mathbf{F}_I^i = \mathbf{F}_N^i + \mathbf{F}_T^i$ ) and torque  $\mathbf{T}^i$  from Shabana (2010).

$$\mathbf{Q}_R^i = \begin{bmatrix} Q_x^i \\ Q_y^i \\ Q_z^i \end{bmatrix} = \mathbf{F}_I^i = \begin{bmatrix} F_{N,x} + F_{T,x} \\ F_{N,y} + F_{T,y} \\ F_{N,z} + F_{T,z} \end{bmatrix} \quad (20)$$

$$\mathbf{Q}_\theta^i = -(\mathbf{A}^i \bar{\mathbf{u}}_I^i \bar{\mathbf{G}}^i)^T \mathbf{F}_I^i + (\mathbf{A}^i \bar{\mathbf{G}}^i)^T \mathbf{T}^i \quad (21)$$

$\bar{\mathbf{u}}_I^i = [\bar{x}_I^i \ \bar{y}_I^i \ \bar{z}_I^i]^T$  is the position of contact point I on body i with respect to the coordinate system. The generalized forces are added to the generalized external force vector  $\mathbf{Q}_e^i$  in equation (1)

Generalized External Forces acting on Oil sand unit i = 15, 16, ..., 64: The contact forces, and spring damper

forces are the external forces acting on each oil sand unit i as shown in Figure 7. The crawler shoes exert equal and opposite contact forces ( $\mathbf{F}_J^i$ ) and frictional torque ( $\mathbf{T}^i$ ) on oil sand unit i at point J as in Figure 7. Consequently, the generalized forces associated with contact force vector  $\mathbf{F}_J^i$  and friction torque  $\mathbf{T}^i$  on oil sand unit i is given by equations (22) and (23).

$$\mathbf{Q}_R^i = \mathbf{F}_J^i = -\mathbf{F}_I^i \quad (22)$$

$$\mathbf{Q}_\theta^i = -(\mathbf{A}^i \bar{\mathbf{u}}_J^i \bar{\mathbf{G}}^i)^T \mathbf{F}_J^i + (\mathbf{A}^i \bar{\mathbf{G}}^i)^T \mathbf{T}^i \quad (23)$$

$\bar{\mathbf{u}}_J^i = [\bar{x}_J^i \ \bar{y}_J^i \ \bar{z}_J^i]^T$  = position of contact point J on unit i with respect to the body coordinate system shown in Figure 7.

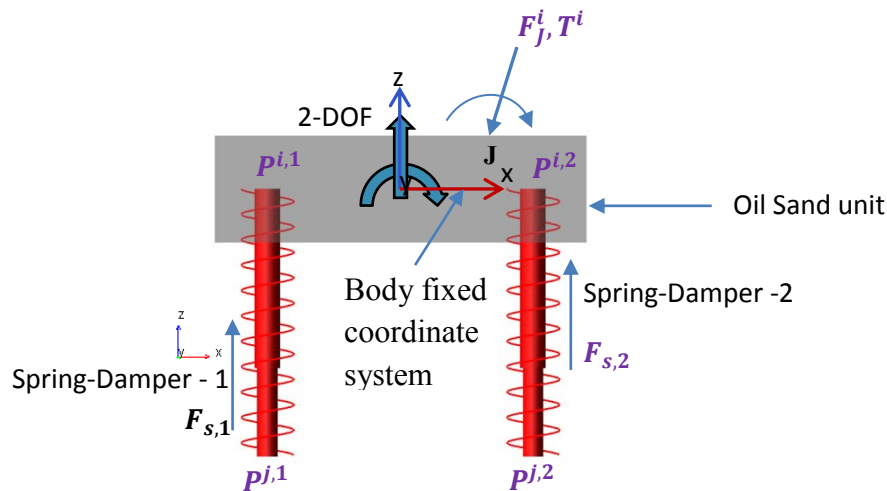


Figure 7 : External forces on Oil Sand unit i

In addition to the contact force, two spring-damper forces are also exerted on the oil sand unit as shown in Figure 7. This spring damper force acts along the line connecting points  $P^{i,1}$  and  $P^{i,2}$  on oil sand unit i to corresponding points  $P^{j,1}$  and  $P^{j,2}$  on default ground link of MSC Adams (Figure 7). The spring damper force  $F_{s,1}$  acting along the line connecting points  $P^{i,1}$  and  $P^{j,1}$  from Shabana (2010) can be expressed as in equation (24).

$$F_{s,1} = k(l_1 - l_o) + c\dot{l}_1 \quad (24)$$

k – spring stiffness; c – damping constant;  $l_1$  – length of spring 1 at any time t;  $l_o$  – undeformed spring length;  $\dot{l}_1$  – time derivative of  $l_1$ ; and the spring coefficient, damping coefficient and length  $l_o$  are listed in Table 3.

Table 3: Oil Sand Properties

Stiffness (k), (MN/m)	Damping (c), (kN-s/m)	Spring length (l <sub>o</sub> ), (m)
20	120	5.0

The generalized forces associated with spring force  $F_{s,1}$  can be derived from Shabana (2010) as in equations (25) and (26)

$$\mathbf{Q}_R^i = {}_{-1}F_{s,1} \hat{\mathbf{r}}_{P,1}^{ij} \quad (25)$$

$$\mathbf{Q}_{\theta,1}^i = F_{s,1} (\mathbf{A}^i \tilde{\mathbf{u}}_{P,1}^i \bar{\mathbf{G}}^i)^T \hat{\mathbf{r}}_{P,1}^{ij} \quad (26)$$

$$\hat{\mathbf{r}}_{P,1}^{ij} = \frac{\mathbf{r}_{P,1}^{ij}}{l_1} = \text{unit vector along the line of action of force } F_{s,1} \quad (27)$$

$$\mathbf{r}_{P,1}^{ij} = \mathbf{r}_{P,1}^i - \mathbf{r}_{P,1}^j \quad (28)$$

$\mathbf{r}_{P,1}^i$  is the global position vector of point  $P^{i,1}$  on oil sand unit  $i$ ;  $\mathbf{r}_{P,1}^j$  is the global position vector of point  $P^{j,1}$  on default ground in MSC ADAMS;

$\bar{\mathbf{u}}_{P,1}^i = [\bar{x}_{P,1}^i \ \bar{y}_{P,1}^i \ \bar{z}_{P,1}^i]$  is the position of contact point  $P^{i,1}$  on oil sand unit  $i$  with respect to its body coordinate system. Similarly, the generalized forces can be derived for the spring damper-2 system shown in Figure 7. These generalized forces are added to the generalized external force vector  $\mathbf{Q}$  in equation (1).

*Generalized Constraint Forces acting on crawler shoe and oil sand unit  $i$ :* The crawler shoe  $j$  is connected to crawler shoe  $i-1$  and  $i+1$  by four joints (two spherical and two parallel primitive joints) as shown in Figure 4. Similarly an oil sand unit  $i$  is connected to four adjacent oil sand units by two spherical joints and two inplane primitive joints as defined in the kinematics part of this paper. The generalized constraint forces are obtained using Lagrange multipliers ( $\lambda$ ) defined in Shabana [14, 15] and can be expressed in general form as in equation 29.

$$\mathbf{Q}_c^i = -\mathbf{C}_q^T \lambda \quad (29)$$

In equation (29),  $\mathbf{C} = \mathbf{C}(\mathbf{q}, t)$  is the vector of system kinematic constraint equations (both joint and driving constraints) and  $\lambda$  is the corresponding vector of system Lagrange multipliers. The number of Lagrange multipliers in the vector  $\lambda$  = total number of constraint equations in the vector  $\mathbf{C}(\mathbf{q}, t) = n_c = 346$  or  $347$  as defined in kinematics part of this paper. Substituting the expression for  $\mathbf{Q}_c^i$  into equation (1), the equation of motion for part  $i$  is given by equation (30).

$$\mathbf{M}^i \ddot{\mathbf{q}}^i + \mathbf{C}_q^T \lambda = \mathbf{Q}_e^i + \mathbf{Q}_v^i \quad (i = 2, 3, 4, \dots, 64) \quad (30)$$

For  $n_b = 63$  interconnected rigid multi-body system shown in Figure 2, the differential equations of motion can be written from Shabana (2010) as in equation (31).

$$\mathbf{M} \ddot{\mathbf{q}} + \mathbf{C}_q^T \lambda = \mathbf{Q}_e + \mathbf{Q}_v \quad (31)$$

$$\mathbf{M} = \begin{bmatrix} \mathbf{M}^2 & & & \\ & \mathbf{M}^3 & & \mathbf{0} \\ \mathbf{0} & & \ddots & \\ & & & \mathbf{M}^{64} \end{bmatrix}; \mathbf{C}_q^T = \begin{bmatrix} \mathbf{C}_{q^2}^T \\ \mathbf{C}_{q^3}^T \\ \vdots \\ \mathbf{C}_{q^{64}}^T \end{bmatrix}; \mathbf{Q}_e = \begin{bmatrix} \mathbf{Q}_e^2 \\ \mathbf{Q}_e^3 \\ \vdots \\ \mathbf{Q}_e^{64} \end{bmatrix}; \text{ and } \mathbf{Q}_v = \begin{bmatrix} \mathbf{Q}_v^2 \\ \mathbf{Q}_v^3 \\ \vdots \\ \mathbf{Q}_v^{64} \end{bmatrix} \quad (32)$$

The total number of differential equations in equation (31) is  $6 \times n_b = 6 \times 14 = 378$ , while the number of unknowns are the sum of  $n = 6 \times n_b = 378$  generalized accelerations and  $n_c = 346$  or  $347$  Lagrange multipliers. From Shabana (2010), the additional  $n_c$  equations needed to solve for  $n + n_c$  unknowns are obtained from kinematic constraint acceleration equation defined in Frimpong and Thiruvengadam (2015) and by equation (33). Equations (31) and (33) can be combined and can be expressed in matrix form as in equation (34).

$$\mathbf{C}_q \ddot{\mathbf{q}} = \mathbf{Q}_d \quad (33)$$

$$\begin{bmatrix} \mathbf{M} & \mathbf{C}_q^T \\ \mathbf{C}_q & \mathbf{0} \end{bmatrix} \begin{bmatrix} \ddot{\mathbf{q}} \\ \lambda \end{bmatrix} = \begin{bmatrix} \mathbf{Q}_e + \mathbf{Q}_v \\ \mathbf{Q}_d \end{bmatrix} \quad (34)$$

The above system of differential algebraic equations is solved numerically using MSC ADAMS to predict motion parameters and reaction forces.

#### IV. SOLUTIONS TO THE DYNAMIC EQUATIONS

Adams numerical procedure is verified by solving a simple two-body dynamic problem analytically and

comparing the analytical results with the numerical results obtained by solving the same problem with MSC ADAMS. A two-body dynamic problem in which a rectangular block whose dimensions and mass properties are within the same order of magnitude as the crawler shoe is assumed to slide on a flat rectangular terrain. The flat terrain is in turn fixed to the ground. The rectangular block and flat plane interact through contact forces. The objective of this problem is to determine the generalized accelerations, joint reaction forces and driving constraint forces analytically for given initial conditions at time  $t$ , as shown in Figure 8.

In this multi-body system, the flat plane and rectangular block are labelled as body 2 and body 3 in Figure 8. respectively. The global and centroidal body coordinate systems are also shown in Figure 8. The dimension of the flat terrain is 30m x 1m x 10m and that of the rectangular block is 0.5m x 0.5m x 3.5 m. The densities of rectangular block and flat terrain are assumed to be same as the density of crawler shoe (Table 1)

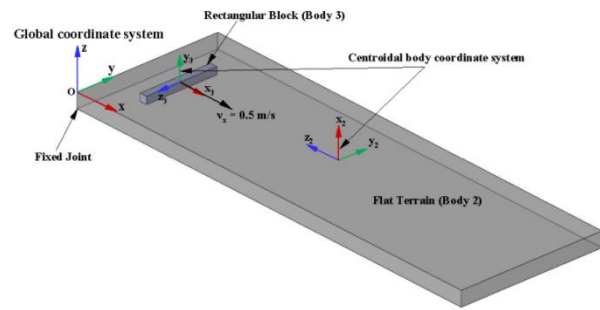


Figure 8 : Schematic of the two body dynamic problem

This two-body system has twelve absolute Cartesian coordinates. The vector of system generalized coordinates from Shabana (2010) is expressed as in equation (35). The absolute velocity vector can be written as equation (36). At time  $t = 0$ , the system generalized coordinates and velocity vector are defined by equations (37) and (38).

$$\mathbf{q} = [\mathbf{q}^2 \quad \mathbf{q}^3]^T = [R_x^2 \quad R_y^2 \quad R_z^2 \quad \phi^2 \quad \theta^2 \quad \psi^2 \quad R_x^3 \quad R_y^3 \quad R_z^3 \quad \phi^3 \quad \theta^3 \quad \psi^3]^T \quad (35)$$

$$\dot{\mathbf{q}} = [\dot{R}_x^2 \quad \dot{R}_y^2 \quad \dot{R}_z^2 \quad \dot{\phi}^2 \quad \dot{\theta}^2 \quad \dot{\psi}^2 \quad \dot{R}_x^3 \quad \dot{R}_y^3 \quad \dot{R}_z^3 \quad \dot{\phi}^3 \quad \dot{\theta}^3 \quad \dot{\psi}^3]^T \quad (36)$$

$$\mathbf{q}(t=0) = [15.0 \quad 5 \quad -0.5 \quad 3\pi/2 \quad \pi/2 \quad \pi/2 \quad 3.25 \quad 5.0 \quad 0.25 \quad 0 \quad \pi/2 \quad 0]^T \quad (37)$$

$$\dot{\mathbf{q}}(t=0) = [0 \quad 0 \quad 0]^T \quad (38)$$

Body 2 is fixed to the ground using fixed joint as shown in Figure 8 and has zero degrees of freedom. The position and orientation of the centroidal coordinate system of body 2 shown in Figure 8 are fixed with respect to the global coordinate system. The six constraint equations for body 2 can be written as equation (39) from Shabana (2010).

$$C_1(\mathbf{q}, t) = R_x^2 - 15.0 = 0$$

$$C_2(\mathbf{q}, t) = R_y^2 - 5.0 = 0$$

$$C_3(\mathbf{q}, t) = R_z^2 + 0.5 = 0$$

$$C_4(\mathbf{q}, t) = \phi^2 - \frac{3\pi}{2} = 0 \quad (39)$$

$$C_5(\mathbf{q}, t) = \theta^2 - \frac{\pi}{2} = 0$$

$$C_6(\mathbf{q}, t) = \psi^2 - \frac{\pi}{2} = 0$$

The constraint equations for body 2 can be written in a vector form as equation (40) and the corresponding vector of Lagrange Multipliers as equation (41).

$$\mathbf{C}^2(\mathbf{q}, t) = [C_1(\mathbf{q}, t) \quad C_2(\mathbf{q}, t) \quad C_3(\mathbf{q}, t) \quad C_4(\mathbf{q}, t) \quad C_5(\mathbf{q}, t) \quad C_6(\mathbf{q}, t)]^T \quad (40)$$

$$\boldsymbol{\lambda}^2 = [\lambda_1 \quad \lambda_2 \quad \lambda_3 \quad \lambda_4 \quad \lambda_5 \quad \lambda_6]^T \quad (41)$$

Body 3 is constrained to move in the x-direction with a constant velocity of 0.5 m/s without changing its orientation. But it can move freely in z and y-directions. The required driving force is assumed to act at the centroid of body 3. The four driving constraint equations

for body 3 are given by equation (42). The vector of constraint equations for body 3 is given by equation (43) and the corresponding vector of Lagrange multipliers is also given by equation (44).

$$\begin{aligned}
 C_7(\mathbf{q}, t) &= R_x^3 - 3.25 - 0.5 * t = 0 \\
 C_8(\mathbf{q}, t) &= \phi^3 = 0 \\
 C_9(\mathbf{q}, t) &= \theta^3 - \frac{\pi}{2} = 0 \\
 \mathbf{C}(\mathbf{q}, t) &= [\mathbf{C}^2(\mathbf{q}, t) \quad \mathbf{C}^3(\mathbf{q}, t)]^T \text{ or} \\
 C_{10}(\mathbf{q}, t) &= \psi^3 = 0
 \end{aligned}$$

$$\lambda^3 = [\lambda_7 \quad \lambda_8 \quad \lambda_9 \quad \lambda_{10}]^T \tag{44}$$

The vector of system constraint equations and Lagrange multipliers are given by equations (45) and (46). There are twelve absolute coordinates and ten constraint equations and hence the degree of freedom for this simple system is two.

$$\mathbf{C}^3(\mathbf{q}, t) = [C_7(\mathbf{q}, t) \quad C_8(\mathbf{q}, t) \quad C_9(\mathbf{q}, t) \quad C_{10}(\mathbf{q}, t)]^T \tag{43}$$

$$\mathbf{C}(\mathbf{q}, t) = [C_1(\mathbf{q}, t) \quad C_2(\mathbf{q}, t) \quad C_3(\mathbf{q}, t) \quad C_4(\mathbf{q}, t) \quad C_5(\mathbf{q}, t) \quad C_6(\mathbf{q}, t) \quad C_7(\mathbf{q}, t) \quad C_8(\mathbf{q}, t) \quad C_9(\mathbf{q}, t) \quad C_{10}(\mathbf{q}, t)]^T \tag{45}$$

$$\lambda = [\lambda^2 \quad \lambda^3]^T = [\lambda_1 \quad \lambda_2 \quad \lambda_3 \quad \lambda_4 \quad \lambda_5 \quad \lambda_6 \quad \lambda_7 \quad \lambda_8 \quad \lambda_9 \quad \lambda_{10}] \tag{46}$$

The free-body diagram of flat plane (Body 2) and rectangular block (Body 3) is shown in Figures 9 and 10. Due to fixed joint constraints (Figure 9), the orientation of body 2 coordinate system vector with

respect to the global coordinate system  $\theta = [\phi \quad \psi]^T$  at any time is equal to the initial orientation at  $t = 0$ . Thus, the time rate of change of  $\theta^2$  is also equal to zero.

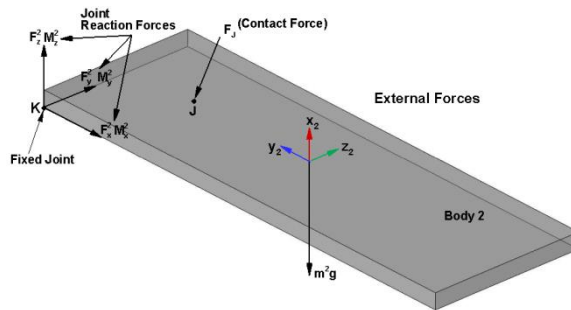


Figure 9: Free-body diagram of flat plane (body 2)

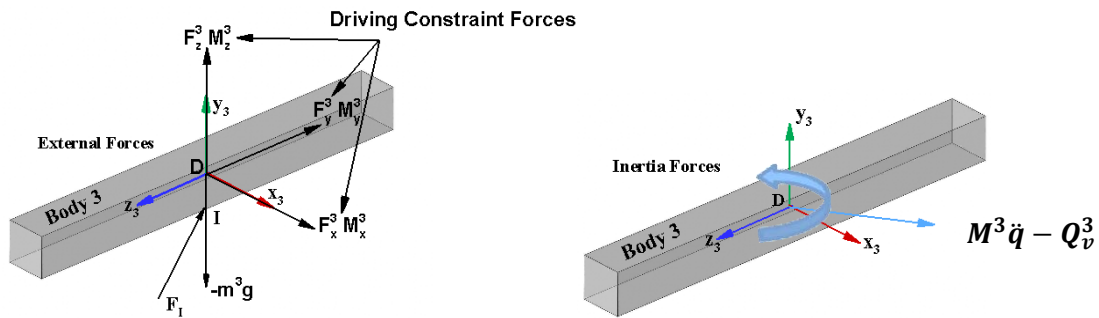


Figure 10: Free-body diagram of rectangular block (body 3)

Similarly due to driving constraints the orientation of the body 3,  $\theta^3 = [\phi^3 \quad \theta^3 \quad \psi^3]^T$  does not change with time. Therefore,  $\dot{\theta}^3(t) = \dot{\theta}^3(t=0) = [0 \quad \pi/2 \quad 0]^T$  for any given time. Since  $\theta^3(t)$  is fixed with respect to time  $\ddot{\theta}^3(t) = [0 \quad 0 \quad 0]^T$ .

The mass inertia matrix of body 2 and body 3 are given in Table 4.

Table 4 : Mass and Inertia tensor of Body 2 and Body 3

Body 2	$m^2$ (kg)	$\bar{I}_{\theta\theta}^2$ (kg.m <sup>2</sup> )		
	2.3403 x 10 <sup>6</sup>	1.95025E+008	0	0
0		1.75717525E+008	0	
0		0	1.9697525E+007	
Body 3	$m^3$ (kg)	$\bar{I}_{\theta\theta}^3$		
	6825.875	7110.2864583	0	0
0		7110.2864583	0	
0		0	284.4114583	

The rectangular block (body 3) sinks vertically to the ground ( body 2) and hence  $F_{N,x} = F_{N,y} = 0$ . The values of the penetration ( $x$ ) and penetration velocity ( $\dot{x}$ ) in equation (17) to calculate normal force ( $F_N$ ) and slip velocities ( $V_s$ ) in equation (18) to calculate tangential forces ( $F_T$ ) at any time t are obtained by simulating the schematic model in Figure 8 in MSC

ADAMS. These values are shown in Table 5 for t = 0.5s. The friction parameters used in the tangential force calculation are listed in Table 6. It can be seen from Table 5 that the tangential forces  $F_{T,y} = F_{T,z} = 0$  since slip velocities in y and z directions,  $V_{s,y} = V_{s,z} = 0$ .

Table 5 : Contact Force calculation at t = 0.5s using MSC ADAMS

Normal Force (N)		Tangential Force (N)		
Penetration Depth (x), m	Penetration Velocity ( $\dot{x}$ ), m/s	Slip Velocities (m/s)		
		$V_{s,x}$	$V_{s,y}$	$V_{s,z}$
-0.0208	-0.1011	0.5	0	0

Table 6 : Friction Parameters for the Analytical Study [28, 29]

Static Friction Coefficient ( $\mu_s$ )	Dynamic Friction Coefficient ( $\mu_d$ )	Static Transition velocity ( $V_{st}$ , m)	Dynamic Transition velocity ( $V_d$ , m)
0.3	0.1	0.0001	0.01

The contact force vector on body 2 is equal and opposite to that of body 3 as shown in Figure 9 ( i.e.  $F_J^2 = -F_J^3$  ).

The data used to obtain mass matrix  $M$  Jacobian of the kinematic constraints  $C_q$ , generalized external forces  $Q_e$  and generalized quadratic velocity vector  $Q_c$  in equation (31) for body 2 and body 3 are listed in Table 7.

Table 7 : Data used in equation (31)

Body 2	$M^2$	2.340E6	0	0	0	0	0
		0	2.340E6	0	0	0	0
		0	0	2.340E6	0	0	0
		0	0	0	1.9503E8	0	0
		0	0	0	0	1.75718E8	0
		0	0	0	0	0	1.96975E7
	$Q_e^{2T}$	0	0	-23002618	0	5091625	0
	$C_{q^2}$	1	0	0	0	0	0
		0	1	0	0	0	0
		0	0	1	0	0	0
		0	0	0	1	0	0
		0	0	0	0	1	0
		0	0	0	0	0	1
0		0	0	0	0	0	
0		0	0	0	0	0	
0		0	0	0	0	0	
$Q_v^{2T}$	0	0	0	0	0	0	
Body 3	$M^3$	6825.875	0	0	0	0	0
		0	6825.875	0	0	0	0
		0	0	6825.875	0	0	0
		0	0	0	7110.28646	0	0
		0	0	0	0	7110.28646	0
		0	0	0	0	0	284.41146
	$Q_e^{3T}$	0	0	-23002618	0	5091625	0
	$C_{q^3}$	0	0	0	0	0	0
		0	0	0	0	0	0
		0	0	0	0	0	0
		0	0	0	0	0	0
		0	0	0	0	0	0
		0	0	0	0	0	0
		1	0	0	0	0	0
		0	0	0	0	1	0
0		0	0	0	0	1	
$Q_v^{3T}$	0	0	0	0	0	0	

Using  $C_q = [C_{q^2} \ C_{q^3}]$  from equation (32) substituted in to equation 34 and solved for  $\mathbf{q}$  and  $\lambda$ . and equation 45, it can be shown that  $Q_d = \mathbf{0}$  in The results are listed in Tables 8 and 9. equation 33. The data from Table 7 and  $Q_{d..} = \mathbf{0}$  are

Table 8 : Solution for  $\ddot{\mathbf{q}}$

$\ddot{\mathbf{q}}$	$\ddot{R}_x^2$ (m/s <sup>2</sup> )	$\ddot{R}_y^2$ (m/s <sup>2</sup> )	$\ddot{R}_z^2$ (m/s <sup>2</sup> )	$\ddot{\phi}^2$ (d/s <sup>2</sup> )	$\ddot{\theta}^2$ (d/s <sup>2</sup> )	$\ddot{\psi}^2$ (d/s <sup>2</sup> )	$\ddot{R}_x^3$ (m/s <sup>2</sup> )	$\ddot{R}_y^3$ (m/s <sup>2</sup> )	$\ddot{R}_z^3$ (m/s <sup>2</sup> )	$\ddot{\phi}^3$ (d/s <sup>2</sup> )	$\ddot{\theta}^3$ (d/s <sup>2</sup> )	$\ddot{\psi}^3$ (d/s <sup>2</sup> )
	0	0	0	0	0	0	0	0	-3.3236521	0	0	0

Table 8 : Solution for  $\ddot{\mathbf{q}}$

$\ddot{\mathbf{q}}$	$\ddot{R}_x^2$ (m/s <sup>2</sup> )	$\ddot{R}_x^3$ (m/s <sup>2</sup> )	$\ddot{R}_x^3$ (m/s <sup>2</sup> )	$\ddot{\phi}^2$ (d/s <sup>2</sup> )	$\ddot{\theta}^2$ (d/s <sup>2</sup> )	$\ddot{\psi}^2$ (d/s <sup>2</sup> )	$\ddot{R}_x^3$ (m/s <sup>2</sup> )	$\ddot{R}_y^3$ (m/s <sup>2</sup> )	$\ddot{R}_z^3$ (m/s <sup>2</sup> )	$\ddot{\phi}^3$ (d/s <sup>2</sup> )	$\ddot{\theta}^3$ (d/s <sup>2</sup> )	$\ddot{\psi}^3$ (d/s <sup>2</sup> )
	0	0	0	0	0	0	0	0	-3.3236521	0	0	0

Table 9 : Solution for  $\lambda$

$\lambda$	$\lambda_1$ (N)	$\lambda_2$ (N)	$\lambda_3$ (N)	$\lambda_4$ (Nm)	$\lambda_5$ (Nm)	$\lambda_6$ (Nm)	$\lambda_7$ (N)	$\lambda_8$ (Nm)	$\lambda_9$ (Nm)	$\lambda_{10}$ (Nm)
	0	0	-23002618	0	509162.5	0	-4427.5	0	0	-1106.875

Generalized Constraint Forces

Using the vector  $\lambda$  in Table 9, the generalized constraint forces for body 2 and body 3 is given by equation (47) from Shabana (2010). These force values are listed in Table 10.

$$\mathbf{Q}_c^2 = \left[ \left( \mathbf{Q}_c^2 \right)_R \quad \left( \mathbf{Q}_c^2 \right)_\theta \right]^T = -[\lambda_1 \quad \lambda_2 \quad \lambda_3 \quad \lambda_4 \quad \lambda_5 \quad \lambda_6]^T$$

$$\mathbf{Q}_c^3 = \left[ \left( \mathbf{Q}_c^3 \right)_R \quad \left( \mathbf{Q}_c^3 \right)_\theta \right]^T = -[\lambda_7 \quad 0 \quad 0 \quad \lambda_8 \quad \lambda_9 \quad \lambda_{10}]^T$$
(47)

Table 10 : Generalized Constraint Forces

		$\left( \mathbf{Q}_c \right)_R^T$ (N)			$\left( \mathbf{Q}_c \right)_\theta^T$ (N-m)		
<b>Body 2</b>	$\mathbf{Q}_c^{2T}$	0	0	23002618	0	-509162.5	0
<b>Body 3</b>	$\mathbf{Q}_c^{3T}$	4427.5	0	0	0	0	1106.875

Actual Fixed Joint Forces on body 2

The actual reaction forces  $\mathbf{R}^2 = \left[ \mathbf{F}^2 \quad \mathbf{M}^2 \right]^T$  where  $\mathbf{F}^2$  and  $\mathbf{M}^2$  are joint reaction forces and moments in the global x, y, and z directions at the fixed

joint (point K) shown in Figure 9 for body 2 can be found using generalized constraint forces. From Shabana (2010),

$$\mathbf{F}^2 = \left[ F_x^2 \quad F_y^2 \quad F_z^2 \right]^T = \left( \mathbf{Q}_c^2 \right)_R$$

$$\mathbf{M}^2 = \left[ M_x^2 \quad M_y^2 \quad M_z^2 \right]^T = -\mathbf{u}_K^2 \times \left( \mathbf{Q}_c^2 \right)_R + \left( \mathbf{G}^{2T} \right)^{-1} \left( \mathbf{Q}_c^2 \right)_\theta$$

$$\mathbf{u}_K^2 = \mathbf{A}^2 \bar{\mathbf{u}}_K^2, \bar{\mathbf{u}}_K^2 = [-15.0 \quad -5.0 \quad -0.5]^T \text{ and } \mathbf{G}^{2T} = \left( \mathbf{A}^2 \bar{\mathbf{G}}^2 \right)^T$$
(48)

Actual Driving Forces on body 3

Similarly the actual driving forces  $\mathbf{D}^3 = \left[ \mathbf{F}^3 \quad \mathbf{M}^3 \right]^T$  where  $\mathbf{F}^3$  and  $\mathbf{M}^3$  are driving forces and moments at point D for body 3 (Figure 10) can be obtained from the generalized driving constraint forces  $\mathbf{Q}_c^3$ :

moments at point D for body 3 (Figure 10) can be obtained from the generalized driving constraint forces  $\mathbf{Q}_c^3$ :

From Shabana (2010),  $\left[ F^3 \quad F^3 \quad F^3 \right]^T \quad \left( \mathbf{Q}^3 \right)$

$$\mathbf{M}^3 = \left[ M_x^3 \quad M_y^3 \quad M_z^3 \right]^T = -\mathbf{u}_D^3 \times \left( \mathbf{Q}_c^3 \right)_R + \left( \mathbf{G}^{3T} \right)^{-1} \left( \mathbf{Q}_c^3 \right)_\theta$$

$$\mathbf{u}_D^3 = \mathbf{A}^3 \bar{\mathbf{u}}_D^3 = \mathbf{0} \text{ since, } \bar{\mathbf{u}}_D^3 = [0 \quad 0 \quad 0]^T \text{ and } \mathbf{G}^{3T} = \left( \mathbf{A}^3 \bar{\mathbf{G}}^3 \right)^T$$
(49)

The fixed joint and driving forces are tabulated in Table 11.

Table 11 : Joint and Driving Forces

	$F_x^2$ (N)	$F_y^2$ (N)	$F_z^2$ (N)	$M_x^2$ (N-m)	$M_y^2$ (N-m)	$M_z^2$ (N-m)
<b>Body 2</b>	0	0	23002618	115013090	-344530107.5	0
<b>Body 3</b>	4427.5	0	0	0	-1106.875	0

The comparison between analytical and simulated values from Adams is summarized in Table 12. The table 12 shows the generalized accelerations on body 2 and body 3, actual reaction forces and moments due to fixed joint on body 2 and driving forces and moments on body 3 at time  $t = 0.5$  s. It can be seen

from Table 12, the absolute value of maximum error between the analytical solution and Adams simulated results is within 2%. Hence Adams can be used with confidence for simulating complex multi-body dynamic simulation problems.

Table 12 : Comparison between Analytical and MSC Adams results at  $t = 0.5$ s

Quantities	Body 2			Body 3		
	Analytical	Adams	Error (%)	Analytical	Adams	Error (%)
$a_x$ (m/s <sup>2</sup> )	0	0		0	0	0
$a_y$ (m/s <sup>2</sup> )	0	0		0	0	0
$a_z$ (m/s <sup>2</sup> )	0	0		-3.3236521	-3.3846	-1.83376
$F_x$ (N)	0	0		4427.5	4383.5822	0.991932
$F_y$ (N)	0	0		0	0	
$F_z$ (N)	23002618	22994000	0.037465	0	0	
$M_x$ (N-m)	115013090	114970000	0.037465	0	0	
$M_y$ (N-m)	-344530107.5	-344410000	0.034861	-1106.875	-1095.5246	1.025446
$M_z$ (N-m)	0	0		0	0	0

The differential algebraic equations (DAE) for the complex crawler-formation interaction given in equation (34) are solved in MSC ADAMS using GSTIFF integrator with I3 formulation [29]. The GSTIFF is a variable-order, variable-step, multi-step integrator based on backward difference formula (BDF). It has maximum integration order of six to calculate solution for the first order ODE's using multi-step predictor-corrector method. The solution methodology for the GSTIFF integrator described below follows the procedure defined in MSC Adams/Solver user manual [29]. In Adams the equations of motion in equation (34) are formulated as

$$\begin{aligned} \mathbf{M}\ddot{\mathbf{q}} + \mathbf{C}_q^T \boldsymbol{\lambda} &= \mathbf{Q}(\mathbf{q}, \dot{\mathbf{q}}, t) \\ \mathbf{C}(\mathbf{q}, t) &= \mathbf{0} \end{aligned} \tag{50}$$

To use GSTIFF integrator equation (50) is converted to first order ODE by introducing a new velocity variable  $\mathbf{u} = \dot{\mathbf{q}}$  [29] in equation (50). This substitution results in equation (51).

$$\begin{aligned} \mathbf{M}(\mathbf{q})\dot{\mathbf{u}} + \mathbf{C}_q^T \boldsymbol{\lambda} - \mathbf{Q}(\mathbf{q}, \mathbf{u}, t) &= \mathbf{0} \\ \mathbf{u} - \dot{\mathbf{q}} &= \mathbf{0} \\ \mathbf{C}(\mathbf{q}, t) &= \mathbf{0} \end{aligned} \tag{51}$$

The index of the DAE is defined as the number of time derivatives required to convert DAEs to a system of ODEs [29]. The equation (50) or (51) is in the default Index 3 (I3) formulation of GSTIFF integrator. Equation (51) can also be written in the form of equation (52)

$$\mathbf{F}(\mathbf{y}, \dot{\mathbf{y}}, t) = \mathbf{0} \tag{52}$$

In equation (52) state vector  $\mathbf{y} = [\mathbf{u}, \mathbf{q}, \boldsymbol{\lambda}]^T$ .

*Predictor Step:* An explicit predictor step is used to obtain the initial guess value of vector  $\mathbf{y}_{n+1}$  at current time  $t_{n+1}$  in equation (52). In this step, Taylor series polynomial of given order is fitted using the past values of vector  $\mathbf{y}$  to obtain  $\mathbf{y}_{n+1}$ .

*Corrector Step:* The corrector equation for the state vector  $\mathbf{y}$  at the current time  $t_{n+1}$  can be obtained from backward difference formula [29] as shown in equation (53).

$$\mathbf{y}_{n+1} = \mathbf{y}_n + h\beta_0\dot{\mathbf{y}}_{n+1} \quad (53)$$

In equation (53)  $\beta_0$  is constant value specific to the order of backward difference formula and  $\dot{\mathbf{y}}_{n+1}$  is

obtained from the previous predictor step. Adams solver uses iterative Newton-Raphson numerical procedure for solving newton difference vector  $\Delta\mathbf{y}$  arising from linearization of equation (52). Using first order Taylor's series, equation (52) can be linearized about  $\mathbf{y} = \mathbf{y}^k$  and  $\dot{\mathbf{y}} = \dot{\mathbf{y}}^k$  at current time  $\dot{\mathbf{y}} = \dot{\mathbf{y}}^k$  to obtain equations (54) and (55).

$$\mathbf{F}(\mathbf{y}, \dot{\mathbf{y}}, t) = \mathbf{F}(\mathbf{y}^k, \dot{\mathbf{y}}^k, t) + \left. \frac{\partial \mathbf{F}}{\partial \mathbf{y}} \right|_{\mathbf{y}^k, \dot{\mathbf{y}}^k} (\mathbf{y} - \mathbf{y}^k) + \left. \frac{\partial \mathbf{F}}{\partial \dot{\mathbf{y}}} \right|_{\mathbf{y}^k, \dot{\mathbf{y}}^k} (\dot{\mathbf{y}} - \dot{\mathbf{y}}^k) = \mathbf{0} \quad (55)$$

$$\mathbf{F}(\mathbf{y}^k, \dot{\mathbf{y}}^k, t) + \left. \frac{\partial \mathbf{F}}{\partial \mathbf{y}} \right|_{\mathbf{y}^k, \dot{\mathbf{y}}^k} \Delta\mathbf{y} + \left. \frac{\partial \mathbf{F}}{\partial \dot{\mathbf{y}}} \right|_{\mathbf{y}^k, \dot{\mathbf{y}}^k} \Delta\dot{\mathbf{y}} = \mathbf{0} \quad (56)$$

Using equation (53), equation (56) can be derived as follows:

$$\mathbf{y} - \mathbf{y}^k = \Delta\mathbf{y} = h\beta_0(\dot{\mathbf{y}} - \dot{\mathbf{y}}^k) = h\beta_0(\Delta\dot{\mathbf{y}}) \quad (56)$$

$$\therefore \Delta\dot{\mathbf{y}} = \frac{1}{h\beta_0} \Delta\mathbf{y}$$

Substituting equation (56) into equation 55 results in equation (57)

$$\left[ \left. \frac{\partial \mathbf{F}}{\partial \mathbf{y}} \right|_{\mathbf{y}^k, \dot{\mathbf{y}}^k} + \frac{1}{h\beta_0} \left. \frac{\partial \mathbf{F}}{\partial \dot{\mathbf{y}}} \right|_{\mathbf{y}^k, \dot{\mathbf{y}}^k} \right] \Delta\mathbf{y} = -\mathbf{F}(\mathbf{y}^k, \dot{\mathbf{y}}^k, t) \quad (57)$$

From equations (51), (52) and (57), equation (58) can be derived as follows:

$$\frac{\partial \mathbf{F}}{\partial \mathbf{y}} = \begin{bmatrix} -\mathbf{Q}_u & \mathbf{M}_q \dot{\mathbf{u}} + \mathbf{C}_{qq}^T \boldsymbol{\lambda} - \mathbf{Q}_q & \mathbf{C}_q^T \\ \mathbf{I} & \mathbf{0} & \mathbf{0} \\ \mathbf{0} & \mathbf{C}_q & \mathbf{0} \end{bmatrix} \text{ and } \frac{\partial \mathbf{F}}{\partial \dot{\mathbf{y}}} = \begin{bmatrix} \mathbf{M} & \mathbf{0} & \mathbf{0} \\ \mathbf{0} & -\mathbf{I} & \mathbf{0} \\ \mathbf{0} & \mathbf{0} & \mathbf{0} \end{bmatrix} \quad (58)$$

Substituting equation (58) into equation (57), equation (59) is obtained as follows:

$$\begin{bmatrix} \frac{\mathbf{M}}{h\beta_0} - \mathbf{Q}_u & \mathbf{M}_q \dot{\mathbf{u}} + \mathbf{C}_{qq}^T \boldsymbol{\lambda} - \mathbf{Q}_q & \mathbf{C}_q^T \\ \mathbf{I} & -\frac{\mathbf{I}}{h\beta_0} & \mathbf{0} \\ \mathbf{0} & \mathbf{C}_q & \mathbf{0} \end{bmatrix}_{\mathbf{y}^k, \dot{\mathbf{y}}^k} \Delta\mathbf{y} = -\mathbf{F}(\mathbf{y}^k, \dot{\mathbf{y}}^k, t) \quad (59)$$

Equation (59) is then solved iteratively using Newton-Raphson algorithm until solution is converged for the current time  $t_{n+1}$ .

*Convergence:* When the value of residue ( $|\mathbf{F}|$ ) and corrections  $|\Delta\mathbf{y}|$  in equation (59) is small, the GSTIFF integrator in MSC Adams estimates local integration error which is a function of difference between the predicted and corrected value, step size  $h$  and the order of integration [29]. When this integration error is less than the specified integration error tolerance in MSC Adams (specified error = 1.0E-003), the solver

proceeds to the next time step. Otherwise the integrator takes a smaller time step and recalculates the solution. This predictor-corrector process is repeated until the simulation end time is reached.

*Stability:* It can be seen in equation (59) when step size  $h$  approaches zero the Jacobian matrix in equation (59) becomes singular. Hence GSTIFF integrator with I-3 formulation becomes unstable at small time steps and hence an alternative formulation that reduces the index of DAEs has to be used. The GSTIFF integrator with SI2 (Stabilized Index - 2) formulation modifies 22 equation

(51) to DAEs with Index 2. This modification stabilizes the DAEs and eliminates the singularity of the SI2 Jacobian matrix when step size  $h$  is closer to zero [29].

### V. RESULTS AND DISCUSSIONS

The crawler track assembly in Figure 2 is modeled in SOLIDWORKS 2013 and the solid model is imported into MSC ADAMS. A 3-D virtual crawler track interacting with oil sands is created in MSC ADAMS to simulate the dynamic propel action of the crawler track for two types of motion constraints. It should be noted that before any propelling operation begins, the oil sand model along with crawler track is allowed to reach its static equilibrium position. From the equilibrium position, the simulation experiment for the 10s period of straight line and turning motion of crawler track on oil sand ground have been carried out to study the linear and angular motion of crawler track, contact forces between crawler shoes and ground and deflection of the *oil sand*

*terrain*. In this paper, only the kinematics (displacement, velocity and accelerations) of crawler shoes are presented. The dynamic results (contact forces, constraint forces and total deformation of oil sand) are presented separately in the force part of this paper.

*Case 1: Only Translation:* The time variation of displacement of center of mass of different crawler shoes in the x, y and z-direction is plotted and is shown in Figure 11. The x-displacement (Figure 11a) follows the motion constraint imposed on crawler shoe 13 while the y and z displacement are determined based on the external forces acting on each crawler shoes during the translation motion. The y-displacement (Figure 11b) shows negligible sliding motion of the crawler track while the time variation of displacement in the z-direction (Figure 11c) shows the vertical bouncing motion from its equilibrium position at time  $t = 0$ .

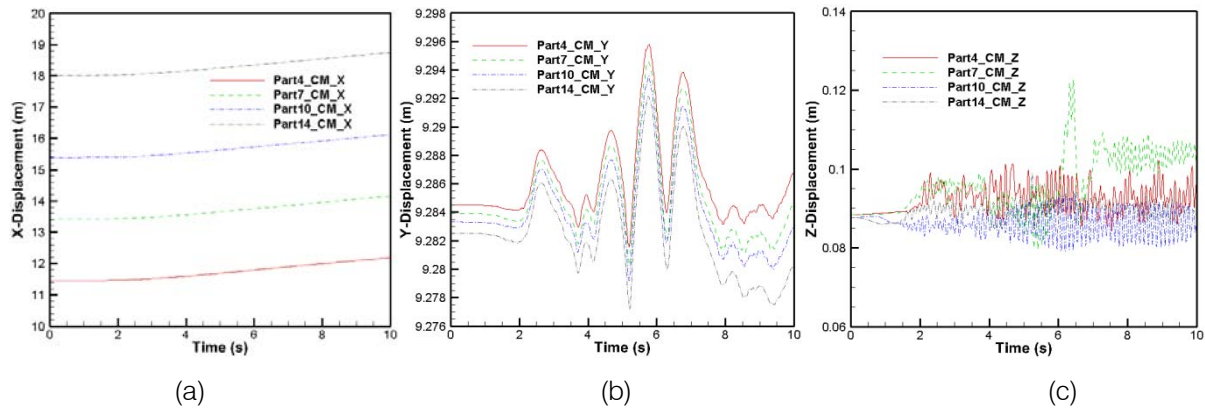


Figure 11 : Displacement of different crawler shoes

The time variation of velocity of different crawler shoes in the x, y and z directions are shown in Figure 12. The x - velocity variation in Figure 12a shows that with the exception of part 14, all other shoes have fluctuating x - velocity variation in time during their translation motion. This is because the longitudinal driving constraint is only applied on part 14 while other

crawler shoes x-velocity behavior are also influenced by external and joint forces. The lateral sliding velocity (y-velocity) is the same for all crawler shoes as shown in Figure 12b. The vertical velocity 23 (Figure 12c) also shows fluctuating behavior due to vertical bouncing of crawler track during its propelling motion.

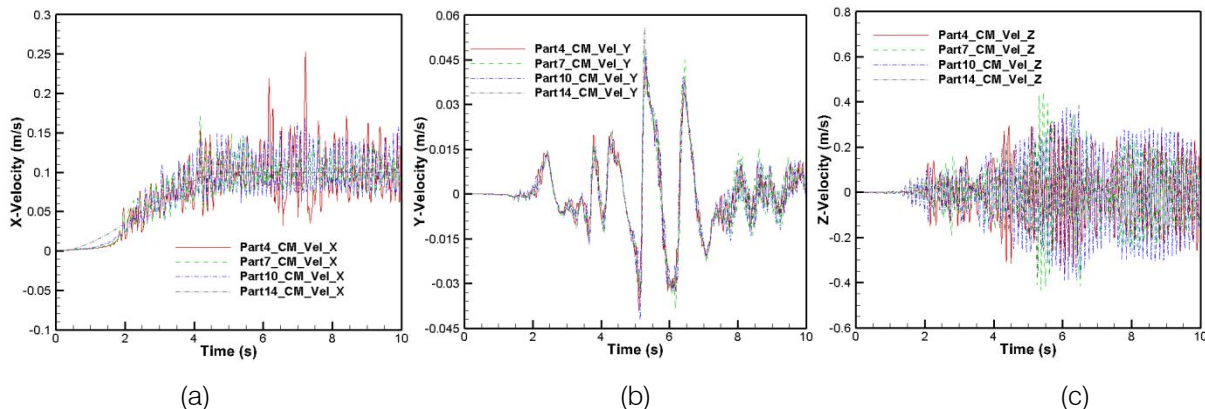


Figure 12 : Velocity of different crawler shoes

The accelerations of different crawler shoes in x, y and z-directions is shown in Figure 13. The acceleration of part 14 in the x-direction is dictated by the driving constraint (maximum acceleration on part 14 is 0.03 m/s<sup>2</sup>), while other parts have large fluctuations in

their values as shown in Figure 13a. The magnitude of acceleration in the y-direction is much smaller in comparison to their values in z-direction as shown in Figures 13b and 13c.

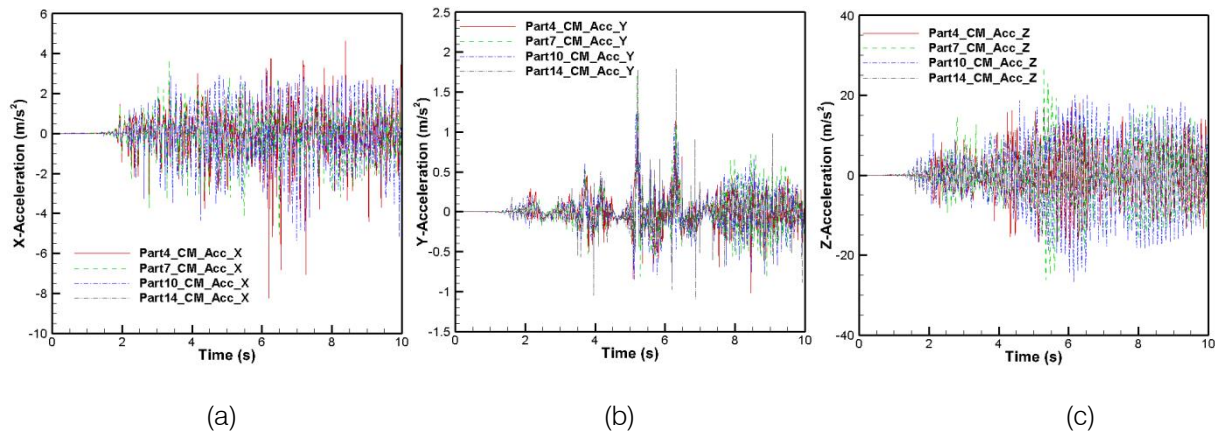


Figure 13 : Acceleration of different crawler shoes

Figure 14 shows the variation of angular velocities in x, y and z directions. It can be seen from Figure 14a that all crawler shoes have same angular velocity variation with time in x-direction and hence the whole crawler track rolls about the x-axis during its propeling motion. This rolling angular velocity attains its peak value when the crawler track attains its specified x-translation velocity (Figure 12a) and decreases thereafter as shown in Figure 14a. The crawler shoes

also rotates about y-axis (joint axis) with large varying angular velocity (Figure 14b) causing relative rotational motion between adjacent shoes of the crawler track. The crawler track also experiences small fluctuating rotational velocities along the global z-direction with average value approximately equal to zero as shown in Figure 14c. This rotation velocity causes crawler track to slide left or right from its direction of motion.

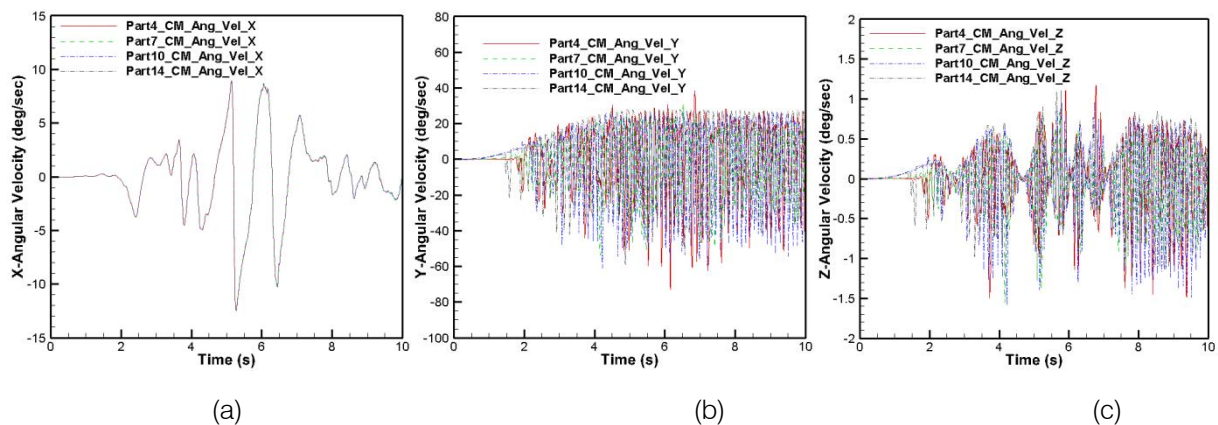


Figure 14 : Angular velocity of different crawler shoes

The time variation of angular accelerations about x, y and z-axes is shown in Figure 15. It can be seen that the whole crawler track rolls back and forth with varying x- angular acceleration as shown in Figure 15a. Due to the fluctuating rotational velocity arising from equivalent revolute joint, the crawler shoes also have unsteady angular acceleration variation about y-axis (Figure 15b). The angular acceleration variation in z-direction (Figure 15c) shows that its average value is approximately zero and hence the crawler track will maintain its straight line motion.

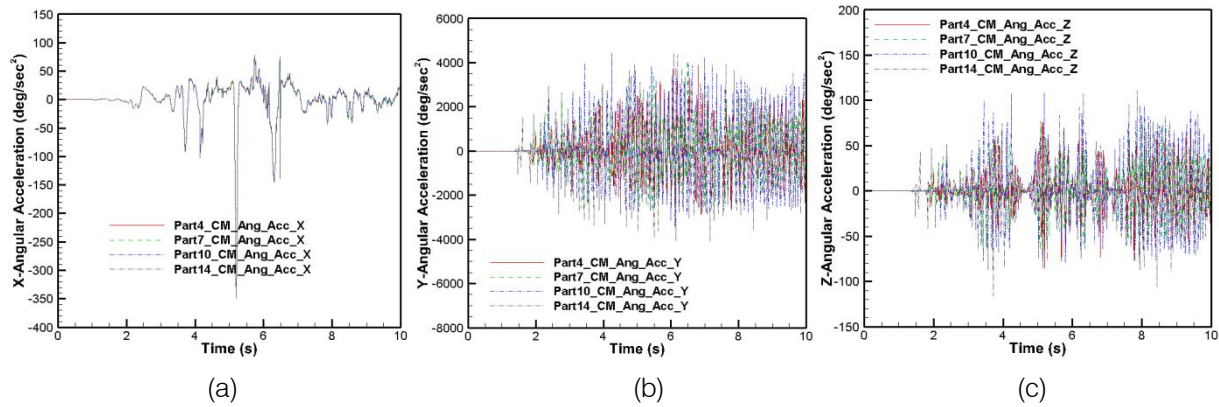


Figure 15 : Angular acceleration of different crawler shoes

Case 2 – Translation and Rotation: In this case the shovel translates and turns with a prescribed velocity as discussed in kinematics part of this paper. Due to space limitations, only results obtained for crawler shoe 9 (Part 10) is plotted and compared with the corresponding results from translation only motion type. The comparison results for other crawler shoes will follow the same general behavior. The time variation of displacement of center of mass of part 10 in x, y and z –

directions is shown in Figure 16. Due to the same translation driving constraint, the x-displacement overlaps with each other. The y-displacement increases due to the sliding action of the crawler track arising from the imposed turning motion. The z-displacement for both motion type exhibits similar behavior except during the middle of the turning motion (between 4.0 – 7.0 s) where the z-displacement show large unsteady behavior as shown in Figure 16c.

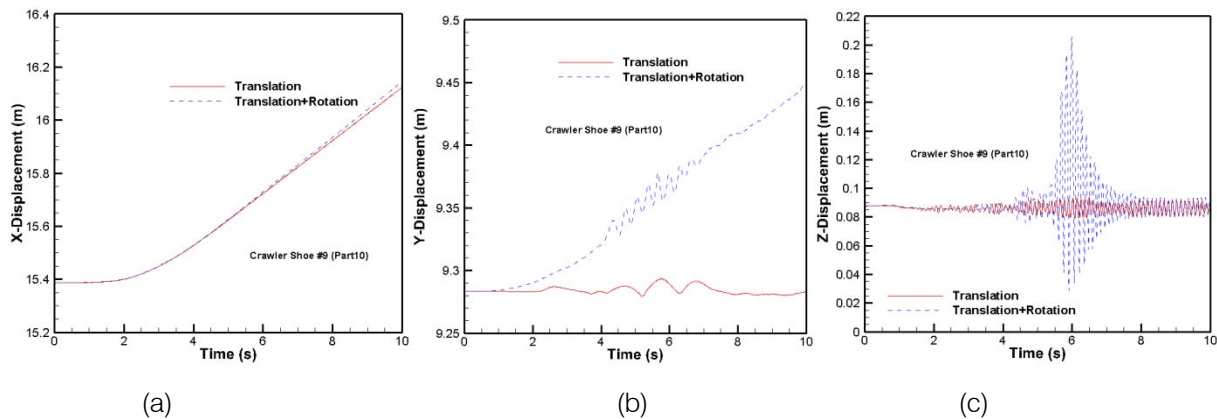


Figure 16 : Displacement of crawler shoe 9

The time variation of velocities in x, y and z directions for crawler shoe 9 for the case of translation and turning motion is shown in Figure 17. The x-velocity variation show similar behavior for both motion types as shown in Figure 17a. The y-velocity (Figure 17b) shows large fluctuations during the middle of the turning motion when compared with translation motion type. This is due to the irregular increase in the lateral displacement of the crawler track (y-displacement in Figure 16b) when the crawler is turning at its prescribed maximum velocities. The unsteady lateral sliding coupled with the flexibility of the oil sand unit causes large amplitude in z-displacement (Figure 16c) and z-velocity (Figure 17c) distributions. This unsteady motion

is brought back to the oscillating steady behavior in less than 3 seconds as shown in Figures 16c, 17b and 17c due to the large damping characteristic of the oil sand terrain.

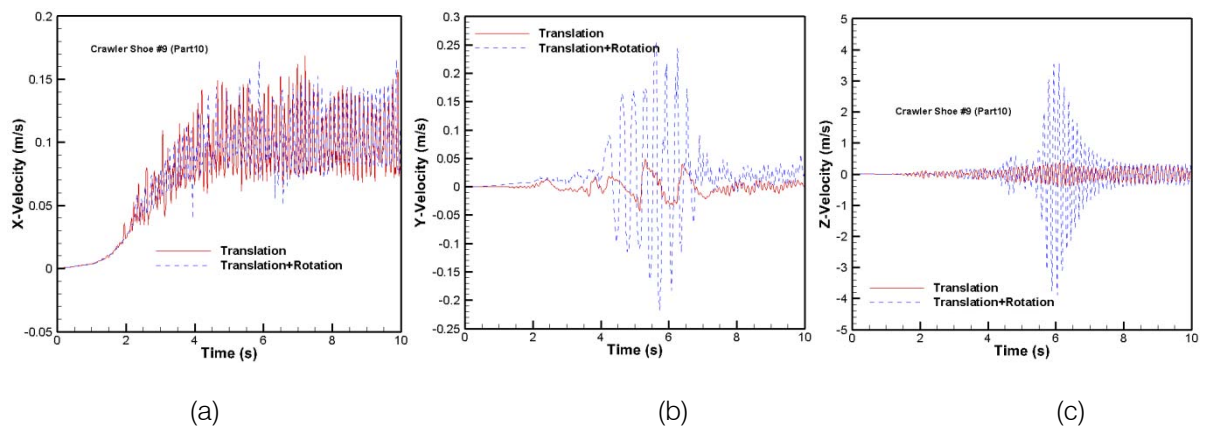


Figure 17 : Velocity of crawler shoe 9

The comparison of time variation of acceleration in x, y and z directions for crawler shoe 9 for both motion types reveal similar general behavior as shown for velocity distributions in Figure 17 and hence not plotted. The angular velocity variation for crawler shoe 9 is shown in Figure 18. The bouncing action of the crawler track also produces simultaneous rolling motion as shown by the angular velocity distribution about x-axis in Figure 18a. But turning motion exhibits increased rolling behavior when compared with translation motion due to

the unsteady lateral sliding of the crawler track. The angular velocity in y-direction shows similar fluctuating behavior for both motion types while the angular velocity about z-axis for turning motion follows the rotation motion constraint (1.0 deg/s) imposed on the moving z-axis of the body fixed motion coordinate system on part 14. The angular acceleration comparison for both motion types also shows similar unsteady behavior as angular velocity (Figure 18) and hence not plotted here.

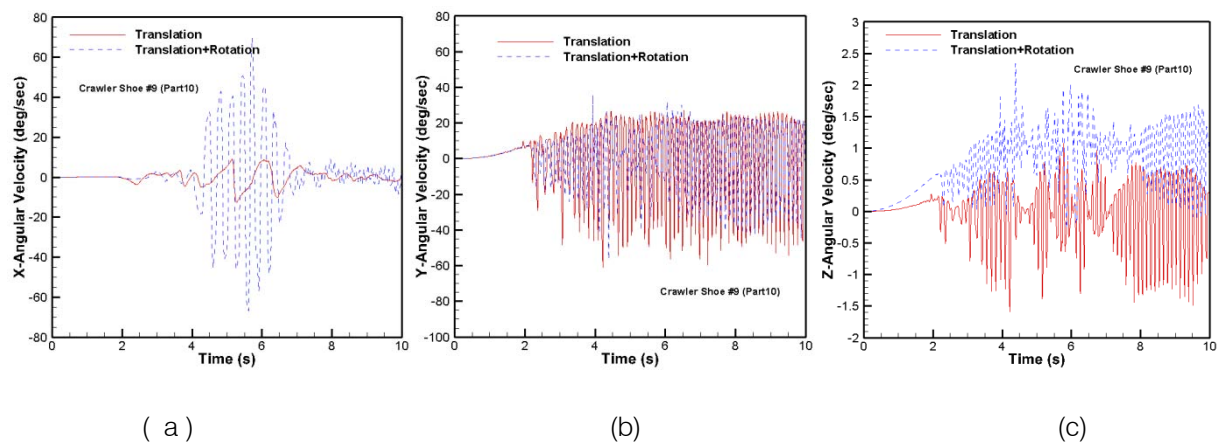


Figure 18 : Angular Velocity of crawler shoe 9

## VI. CONCLUSIONS

The dynamic equation of motion governing the multi-body model of crawler track assembly is obtained to study the propelling motion of crawler track on the oil sand terrain. A simple two-body contact dynamic problem is simulated in MSC Adams and the simulation results for accelerations and constraint forces at a given time is verified by solving the same problem analytically using the dynamic equations of motion and comparing the analytical solution to the simulation results. Subsequent to analytical verification, a rigid 3D virtual prototype model of the crawler track interacting with the

oil sand terrain is developed and simulated in ADAMS environment. The simulation is carried out for the prescribed translation and rotation motion constraints on one of the crawler shoes in the track as reported in the kinematics part of this paper. The interaction between each crawler shoe and ground is modeled using contact force formulation in MSC ADAMS. The kinematic simulation results of the crawler track propelling on the ground for both driving constraints show that in 10 s the crawler slips forward for a maximum longitudinal distance of 0.75 m with vertical

bouncing, lateral sliding and rotation about the x, y and z-axes. For translation motion, the maximum values of lateral sliding and vertical bouncing are 1 cm and 3.5 cm from the equilibrium position. The corresponding maximum sliding and bouncing velocities and accelerations are 0.06 m/s and 0.45 m/s and 1.8 m/s<sup>2</sup> and 27 m/s<sup>2</sup>. The maximum magnitude of angular velocities and accelerations attained about the three orthogonal axes are 12.5 deg/s, 73.0 deg/s and 1.6 deg/s and 350 deg/s<sup>2</sup>, 4420 deg/s<sup>2</sup> and 115 deg/s<sup>2</sup>. For turning motion, these values are 0.5 m and 0.15 m; 0.328 m/s and 4 m/s; and 16 m/s<sup>2</sup> and 290 m/s<sup>2</sup> for lateral and vertical displacement, velocities and accelerations. The maximum magnitude of angular velocities and accelerations about the x, y and z-axes are 70 deg/s, 225 deg/s and 7 deg/s; and 3150 deg/s<sup>2</sup>, 20176 deg/s<sup>2</sup>, and 350 deg/s<sup>2</sup>.

### REFERENCES RÉFÉRENCES REFERENCIAS

- Joy Global Inc., 4100C BOSS Electric Mining Shovel - AC Drive Product Overview, 1-8, 2012. [http://www.phmining.com/MinePro/Literature/Brochures/SUR\\_4100C\\_BOSS\\_AC\\_BRO\\_XS-5491.pdf](http://www.phmining.com/MinePro/Literature/Brochures/SUR_4100C_BOSS_AC_BRO_XS-5491.pdf)
- P&H. 2005. Peak Performance Practices: Lower Works, © P&H MinePro, Milwaukee, WI
- Nakanishi, T. and A.A.Shabana. 1994. Contact forces in the non-linear dynamic analysis of tracked vehicles, *Int. J. for Numerical Methods in Engineering*, Vol., 37: 1251-1275.
- Choi, J.H., Lee, H.C. and A.A. Shabana. 1998. Spatial dynamics of multibody tracked vehicles. Part I: Spatial equations of motion. *Vehicle Systems Dynamics*, Vol. 29: 27-49.
- Lee, H.C., J.H.Choi and A.A.Shabana. 1998. Spatial dynamics of multi-body tracked vehicles II: Contact forces and simulation, *Vehicle Systems Dynamics*, Vol. 29: 113-137.
- Rubinstein, D. and R.Hitron. 2004. A detailed multi-body model for dynamic simulation of off-road tracked vehicles, *Journal of Terramechanics*, 41: 163-173.
- Rubinstein, D., and A.Coppock. 2007. A detailed single-link track model for multi-body dynamic simulation of crawlers, *Journal of Terramechanics*, 44: 355-364.
- Ferrati, G., and R.Girelli. 1999. Modeling and simulation of an agricultural tracked vehicle, *Journal of Terramechanics*, 36: 139-158.
- Ryu, H.S., D.S.Bae, J.H.Choi, and A.A.Shabana. 2000. A compliant track link model for high-speed, high-mobility tracked vehicles, *Int. J. Numer. Meth. Engng*, 48: 1481-1502.
- Madsen, J. 2007. High fidelity modeling and simulation of tracked elements for off-road applications using MSC/ADAMS. <http://sbel.wisc.edu/documents/Independent%20Study%20Report%20final%20edit.pdf>
- Ma, Z. D. and N.C.Perkins. 1999. A hybrid track model for studying dynamic track/sprocket Contact, *Proceedings of the ASME Noise Control and Acoustics Division*: 147-155.
- Frimpong, S., Y.Hu, and K.Awuah-Offei. 2005. Mechanics of cable shovel-formation interactions in surface mining excavations, *Journal of Terramechanics* 42: 15-33.
- Frimpong, S., and Li, Y. 2007. Stress loading of the cable shovel boom under in-situ digging conditions, *Engineering Failure Analysis* 14: 702-715.
- Shabana, A. A. 2010. *Computational dynamics*, 3rd Edition, John Wiley & Sons, NY.
- Shabana, A. A. 1998. *Dynamics of multi-body Systems*, 2nd Edition, Cambridge Univ. Press.
- Edward, J. H. 1989. *Computer aided kinematics and dynamics of mechanical systems*. Allyn and Bacon Series in Engineering.
- Schiehlen, W., N.Guse and R.Seifried. 2006. Multibody dynamics in computational mechanics and engineering applic., *Comput. Methods Appl. Mech. Engrg*. 195: 5509-5522.
- JOY Global Inc.
- Nakanishi, T. and Shabana, A. A., Contact forces in the non-linear dynamic analysis of tracked vehicles, *Int. J. for Numerical Methods in Engineering*, Vol., 37, 1251-1275 (1994).
- Choi, J.H., Lee, H.C. and Shabana, A. A., Spatial dynamics of multibody tracked vehicles Part I: Spatial equations of motion.
- Lee, H.C., Choi, J.H. and Shabana, A. A., Spatial dynamics of multi-body tracked vehicles Part II: Contact forces and simulation results
- Hibbeler, R. C., *Engineering mechanics, dynamics*, 1989, 5th Edition, Macmillan
- Bedford, A. and W.Fowler. 2002. *Eng. Mechanics: Statics and Dynamics*. Prentice Hall.
- Wong, J.Y., *Theory of Ground Vehicles*, 2001, 3rd Edition, John Wiley & Sons, Inc
- Frimpong, S., Li, Y. and Suglo, R., 2013, Dynamic torque and soil deformation mechanics and simulation of the GAP machinery, *J Powder Metall Min S1:002*.
- Lindberg, D., MSC Adams modeling of mechanical system in A400M crew Entrance Door, Master Thesis, Linkoping Institute of Technology, Sweden, 2012.
- Kong, D., Meagher, J.M., Xu, C., Wu, X. and Wu, Y., "Nonlinear contact analysis of gear teeth for malfunction diagnostics," *Proceedings of the IMAC 26th Conference on Structural Dynamics*, Society for Experimental Mechanics, Orlando, Fla, USA, February, 2008.
- MSC. 2014. MSC ADAMS/View help document. © MSC Corporation, San Diego, CA.
- MSC. 2014. MSC ADAMS/Solver help document. © MSC Corporation, San Diego, CA.

30. Frimpong, S., and Thiruvengadam, M. 2015. Rigid multi-body kinematics of shovel crawler-formation interaction, Submitted to Engineering Failure Analysis. \_\_



# GLOBAL JOURNALS INC. (US) GUIDELINES HANDBOOK 2015

---

[WWW.GLOBALJOURNALS.ORG](http://WWW.GLOBALJOURNALS.ORG)